Metasight: High-Resolution NLoS Radar Sensing through Efficient Metasurface Encoding

Timothy Woodford, Kun Qian, Xinyu Zhang
University of California San Diego
{twoodfor,kuq002,xyzhang}@ucsd.edu

ABSTRACT

A large number of traffic collisions occur as a result of non-line-of-sight (NLoS) obstructions. Recent work has explored NLoS automotive radar sensing systems to detect objects in occluded regions. However, current NLoS radars require substantial ambient reflectors, whose size needs to scale with the desired angular resolution and coverage, impeding their deployment in real-world scenarios. In this paper, we propose Metasight, which leverages carefully designed passive millimeter-wave metasurface reflectors and a novel angular encoding scheme to dramatically reduce the reflector size. The Metasight metasurfaces are fully passive, low cost, and can be fabricated by simply using a 3D printer and copper tape. By processing the reflected signals with a robust angle decoding algorithm on the radar, Metasight achieves high NLoS sensing resolution and wide coverage, with an asymptotically higher space-efficiency than conventional natural or artificial reflectors.

CCS CONCEPTS

• **Hardware** → **Wireless devices**; **Sensor applications and deployments**.

KEYWORDS

Passive intelligent surface, metasurface, 3D Printing, automotive sensing, NLoS Radar, around-the-corner radar

ACM Reference Format:
Timothy Woodford, Kun Qian, Xinyu Zhang. 2023. Metasight: High-Resolution NLoS Radar Sensing through Efficient Metasurface Encoding. In *The 21st ACM Conference on Embedded Networked Sensor Systems (SenSys '23), November 12–17, 2023, Istanbul, Turkiye.* ACM, New York, NY, USA, 14 pages. https://doi.org/10.1145/3625687.3625803

1 INTRODUCTION

Non-line-of-sight (NLoS) radar enables intelligent vehicles to see objects hidden behind various obstructions, and is a key technology for improving transportation safety. Studies of real-life driving scenarios indicate that an idealized driver assistance system using only line-of-sight (LoS) sensing technology would still be unable to prevent around 30% of collisions at intersections [5], as well as about 18% of collisions involving pedestrians [22]. Vehicle-to-everything (V2X) radios sharing data between vehicles and infrastructure-mounted sensors have been proposed to create an occlusion-free view of the road environment [37], but this has seen very limited use to date, due to the substantial cost in deploying infrastructure and retrofitting vehicles.

SenSys '23, November 12–17, 2023, Istanbul, Turkiye

ACM ISBN 979-8-4007-0414-7/23/11…$15.00
https://doi.org/10.1145/3625687.3625803

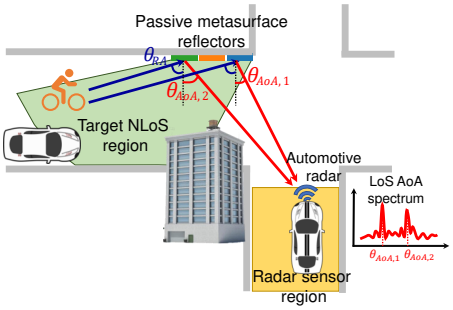

Figure 1: Example usage scenario of Metasight. The Metasight metasurface reflectors encode the NLoS reflection angle θ_{RA} of the target into the LoS AoA spectrum of the radar, for each range-Doppler bin.

By contrast, NLoS sensing does not require cooperating vehicle sensors, and thus can be rapidly deployed. NLoS radar is commonly utilized for transportation sensing applications [32, 48, 56], as they enable NLoS sensing with common roadside objects. Non-radar modalities like optical NLoS sensing only work within a short range, and often require specialized equipment and high illumination power [19, 34, 58].

However, existing NLoS radar systems are limited by their dependence on natural roadside reflectors. These systems either depend on the availability of rich NLoS reflectors immediately near the roadside or path of travel [41, 56]. To enable NLoS sensing in practical environments without rich NLoS opportunities, one needs to leverage multiple small, sparse NLoS reflectors [48, 56], or deploy artificial reflectors [39, 40, 42]. However, sparse NLoS reflections provide relatively limited sensing resolution compared to large NLoS reflectors [56]. On the other hand, our analysis shows that a huge panel reflector (6.3 m in width, § 2.1), with ideal orientation, is needed to achieve an acceptable sensing resolution and angular coverage (§ 2). This is challenging to deploy in practice, as it is hard to ensure the entire panel falls within the radar's LoS.

To overcome these limitations, we propose Metasight, an enhanced artificial reflector that consists of a set of fully passive metasurfaces with beamforming capabilities. As illustrated in Fig. 1, Metasight works by *projecting the radar beamforming function* from the radar itself to the metasurfaces which have a direct view of the occluded NLoS region. The metasurfaces's beamforming patterns are judiciously designed, to enable the radar to sense objects

along a wide range of angles, at a high resolution, without requiring significant space in crowded roadside environments.

The key technique behind Metasight is a space-efficient angular encoding method, which maps an NLoS object's reflection angle (θ_{RA} in Fig. 1) to the LoS angle spectrum ($\theta_{AoA,1}$ and $\theta_{AoA,2}$) observable by the radar. The encoding scheme is enabled by the metasurfaces which *reshape the radar signals into a multi-arm beam pattern covering a discrete set of reflection angles in the target NLoS region*. Compared with planar reflectors [32, 41, 44], Metasight asymptotically reduces the size of the reflectors, from a scale of N to $\log(N)$, where N is the number of discrete angles that together cover the continuous target NLoS region. In practice, the object's location may change continuously and span multiple such angles, so a naive encoding scheme may become highly sensitive to minor ambiguities in the reflection angles. We thus propose a *robust angular encoding* method that bounds the ambiguity within one discrete angle. Furthermore, we design post-processing algorithms that can resolve the ambiguities caused by imperfection of the metasurface beamformers (*e.g.*, sidelobe leakage), or by the far-field approximations in our encoding model. The angle decoding and post-processing can run directly on existing automotive radars without any hardware modification.

The Metasight metasurface is essentially a passive millimeter-wave (mmWave) reflectarray [23] consisting of thousands of unit elements that steer the radar signals to point towards multiple discrete angles. Recent metasurface-assisted sensing systems [12, 25] are made from high-frequency PCBs and active phase shifters (*e.g.*, RF switches), which are expensive and hard to scale. To enable widespread deployment of Metasight, we design a metasurface structure that can be directly fabricated using only a 3D-printed substrate and copper tape. Compared with state-of-the-art passive metasurfaces [29], Metasight avoids the use of specialized electrodeposition equipment, simplifying the fabrication process and reducing the cost, while maintaining a similar level of accuracy in passive reflective beamforming.

We have prototyped Metasight and the angular encoding schemes, using 3D printing and common assembly tools. We have also implemented the signal processing workflow for decoding NLoS objects' angles and locations on a 77 GHz mmWave automotive radar [17]. Our experiments demonstrate that, by using merely three 13×24 cm^2 metasurfaces spanning 0.6 m in total, Metasight can achieve an NLoS angular resolution of 4°. Combined with the range-Doppler profiles, this translates to a location resolution of 35 cm. Metasight's angular resolution and FoV are multi-folds higher/wider than natural planar/curved reflectors. For the same resolution/FoV, its dimension is multi-fold smaller. Our case studies in practical transportation environments also verify that Metasight can satisfy the NLoS sensing requirements of real-world use cases.

To summarize, Metasight makes the following contributions: *(i)* We propose a novel angular encoding method that employs passive metasurfaces to transform NLoS angles into compact LoS angle spectrum, with asymptotically higher space efficiency compared with natural reflectors. *(ii)* We design a new metasurface structure for passive mmWave beamforming, which enables a new fabrication process with significantly lower cost and higher efficiency compared with the state-of-the-art. *(iii)* We implement Metasight and verify its high angle/location resolution in practical transportation scenarios.

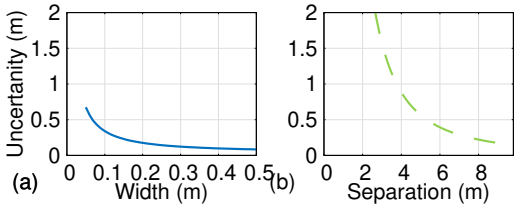

Figure 2: Comparison of the theoretical maximum accuracy of (a) reflection angle-based localization to (b) trilateration localization, for an object at a range of 10 m from the nearest part of the reflector.

2 DESIGN CHOICES FOR NLOS SENSING

Trilateration methods [47, 56] and *reflection angle methods* [32] are two classes of localization methods for NLoS sensing. Trilateration methods pinpoint the target based on the ranges between the target and multiple NLoS reflectors at known locations. Intuitively, the reflectors must be separated sufficiently far apart to dispel their localization ambiguity. In contrast, reflection angle methods measure the range and reflection angle of the target to a single reflector to localize the target. In both cases, the location of the reflector is assumed to be known, and the range from the reflector to the target is found by subtracting the distance from the radar to the reflector from the total range detected by the radar. For example, a small, flat mirror-like object can create a narrow reflecting beam to determine the reflection direction to an object.

We analyze the localization uncertainty numerically using [47], comparing the required width of a flat reflector to the required separation between two trilateration reflectors, with each reflector placed 10 m from the radar. Figure 2 shows that multiple point scatterer reflectors must spread across a region of at least 8.5 m in width, to achieve 0.2 m localization accuracy with the trilateration method. In contrast, only a spreading width of 0.18 m is required by the reflection angle method.

While reflection angle methods exhibit higher location resolution, they require information on surface curvature to determine the signal reflection direction from the incident direction using Snell's law of reflection. Such information is challenging to obtain, especially for non-flat or irregularly shaped reflectors. Furthermore, the curvature of the reflector must be carefully designed to trade off coverage and resolution. In Fig. 3a and 3b, we use cylindrical and flat reflectors to demonstrate these relations. Here the radar can beamform to different parts of the reflectors. $\Delta\theta_{AoA}$ (blue area) and $\Delta\theta_{RA}$ (green area) represent the LoS AoA resolution and the NLoS reflection angle resolution, respectively. With a larger curvature, the cylindrical has a much wider reflection angle coverage, but poorer resolution. In contrast, the flat surface has a higher angle resolution but needs to be much larger to achieve the same coverage. *This creates a three-way trade-off for reflection angle estimation*: we must choose between minimizing the size of the reflector, maximizing the NLoS coverage, and maximizing the NLoS reflection angle resolution.

2.1 Sensing Requirements

Metasight aims to provide a view of a prescribed *target NLoS region*, while the radar has *moved* anywhere within a predefined *sensing region*. For example, for collision avoidance at an intersection (Fig. 1), the sensor region is defined as the lanes of approaching vehicles, up

to a distance determined by the maximum vehicle speed and the time requirement for pre-collision warning, approximately 1.5 s [56]. In such scenarios, the radar should be able to estimate the lane of the occluded vehicle, as well as its approximate speed.

NLoS angle resolution. Determining the current *lane* of an occluded oncoming vehicle is important because certain lanes, such as turning lanes, may not lead to the same collision risk as one-way lanes. Using the 3.3 m lane width standard for urban roads in the US, and assuming we must detect vehicles at least 24 m away from the intersection at a maximum speed of 35 mph [56], we can determine that a NLoS angle resolution of at least $\Delta\theta_{RA} = \frac{3.3m}{24m} \approx 8^\circ$ is required to discriminate the lanes[1].

The NLoS angle resolution also impacts the estimation accuracy of the *speed* of an oncoming vehicle, which is crucial, especially for collision avoidance. A radar estimates the Doppler frequency shift of the received signal. However, it only reveals the radial velocity of the target, $v_\perp = v\cos\varphi$, where v is the actual velocity of the target and ϕ is the angle between the target's moving direction and the direction of the reflector relative to the target. For example, if the vehicle is 4 m from an intersection, within the center lane of a four-lane road, an 8° angle error leads to up to $(\cos 68^\circ - \cos 60^\circ)/\cos 60^\circ = 25\%$ speed estimation error.

NLoS coverage. We denote $\Theta_{RA} = \Delta\theta_{RA}M$ as the NLoS coverage, where M is the number of NLoS angle bins. Then if the reflector is placed on the corner 1 m from the target 2-lane wide NLoS region (Fig. 1), and must sense vehicles 4-24 m away from the intersection, then the required reflection angle range will be $\Theta_{RA} = 51^\circ$, *i.e.*, $M \approx \frac{51^\circ}{8^\circ} \approx 7$.

Reflector size. Similarly, we denote $\Theta_{AoA} = \Delta\theta_{AoA}N$ as the LoS AoA range that covers the reflector and can be used for NLoS localization. Given the distance between the radar and the reflector, denoted as d_{AoA}, the reflector size is $d_{AoA}\Theta_{AoA}$. Suppose the radar's AoA resolution $\Delta\theta_{AoA} = 2^\circ$ and is located 13.2 m (4 lanes) away from the reflector. Assuming that there is a one-to-one mapping between the LoS and NLoS angle bins, *i.e.*, $N = M = 7$, the theoretical minimum width of a natural reflector is $tan(2^\circ) * 13.2m * 7 = 3.2\ m$, even if it has an ideal variable curvature. For a panel reflector (*e.g.*, a wall), the *minimum reflector width needed* becomes 6.3 m! Furthermore, the entire reflector must be visible to the radar, which can hardly be satisfied in practice.

2.2 Overview of Metasight

METASIGHT breaks the dilemma of reflection angle methods using an artificial reflector, which consists of a set of metasurfaces. Each metasurface is intentionally designed to produce one or more narrow reflection beams to cover part of the NLoS region. Upon entering the sensing region, the radar beamforms toward the metasurfaces. Then, the radar may observe multiple "echo" peaks in its angle of arrival (AoA) spectrum, which corresponds to a subset of metasurfaces covering the NLoS target. The radar can then use this AoA spectrum as a signature to *decode* the reflection angles between the metasurface reflectors and each occluded object. Finally, the radar localizes the occluded objects by combining these reflection angles with the range profile.

[1]The derivations in this subsection follow simple geometries based on Fig. 1. The details are omitted due to space constraints.

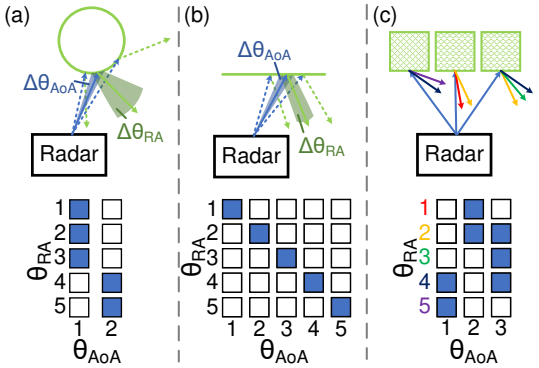

Figure 3: Comparison of a cylindrical reflector, a flat reflector, and Metasight.

We design efficient NLoS angle encoding schemes of the metasurfaces (§ 3) so that the size of the whole artificial reflector can be dramatically reduced, while the desired NLoS coverage and angle resolution are still achieved. We also develop a robust metasurface structure to overcome fabrication inaccuracy (§ 4). To account for the dynamics of the vehicles and the resulting distortions of received signals, we develop a robust decoding process compatible with commercial automotive radars (§ 5).

3 ANGLE ENCODING DESIGN

3.1 Efficient Angle Encoding

The essential limitation of natural reflectors is that they only generate a single dominant specular reflection beam for a given incident plane wave, leading to a linear mapping between LoS AoAs and NLoS reflection angles. Depending on the reflector's curvature, each LoS AoA in the set Θ_{AoA} is mapped to a set of successive reflection angles in the set Θ_{RA}. For example, as shown in Fig. 3, the cylindrical reflector maps one θ_{AoA} value to three θ_{RA} values, due to its low reflection angle resolution. Meanwhile, the flat reflector creates a one-to-one mapping. Yet for both, the radar's AoA range $|\Theta_{AoA}|$, and hence the reflector size, can only scale linearly with the reflection angle range $|\Theta_{RA}|$. Therefore, natural smooth reflectors lack space efficiency and support limited coverage given practical size constraints.

In contrast, in Metasight, we introduce a more *space-efficient* angular coding scheme. Our key idea is to *map each NLoS reflection angle to an LoS AoA spectrum pattern comprised of a subset of LoS AoAs*. With this measure, the reflector size can be significantly reduced, because only N reflecting surfaces can represent 2^N patterns. Physically implementing this mapping entails two requirements. *First*, when an object is at any reflection angle, the radar should observe and only observe the corresponding unique set of dominant LoS AoAs. *Second*, when and only when the radar scans the set of LoS AoAs, the reflector reflects signals to the corresponding reflection angle.

The first requirement is practically achievable since the echos of the radar signal are usually *sparse*. At a specific distance and Doppler frequency, there is usually only one object, corresponding to a single dominant AoA (§ 6.1). Due to this property, it is possible to *encode* each reflection angle with a unique set of LoS AoAs within Θ_{AoA}. The radar observes an AoA spectrum consisting of peaks at a

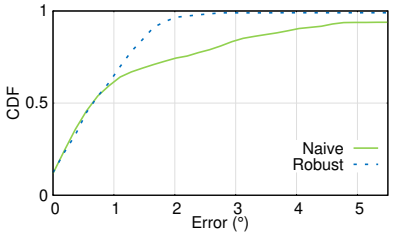

Figure 4: Simulated performance of the robust angular encoding scheme, compared to a naive scheme.

few dominant angles, which are resolvable and only span a smaller angular range to reduce the reflector size. The presence or absence of peaks of N resolvable LoS AoAs forms a N-bit codeword to encode the reflection angle of the target.

For the second requirement, we resort to metasurfaces that can reflect signals to arbitrary directions. With the inhomogeneous surface impedance distribution, a metasurface is no longer constrained by Snell's law of reflection and can redirect beams towards any angle [29]. This stands in contrast to a flat panel reflector [32] that has less than 90° FoV even with infinite width. Metasight uses N metasurfaces that are separated by $\Delta\theta_{AoA}$ and hence resolvable by the radar. Each metasurface reflects incident radar signals into *one or more* highly directional beams, with each beam covering one angle $\theta_{RA} \in \Theta_{RA}$. To ensure the uniqueness of the coding, we assign a unique subset of metasurfaces to cover each reflection angle using one of their reflection beams. Thus, when the radar observes the reflection from a specific subset of metasurfaces, it can decode the corresponding reflection angle of the target without ambiguity. As an example, Fig. 3c shows how we use 3-bit codewords to encode 5 (up to 7) different reflection angles.

We note that this angle coding scheme substantially eases the tradeoff between reflector size and NLoS localization performance. With a standard reflector surface, as shown in Fig. 3a and 3b, the required size of the reflector grows roughly linearly with $|\Theta_{RA}|$, In contrast, with the proposed angle encoding method, we can use N metasurfaces to represent $2^N - 1$ reflection angles at most. So the reflector size, in terms of the number of metasurfaces, grows logarithmically with $|\Theta_{RA}|$, *i.e.*, $\lfloor \log_2 |\Theta_{RA}| \rfloor \Delta\theta_{AoA}$.

3.2 Robust Angular Encoding

The angular coding scheme maps each individual reflection angle to a *subset* of LoS AoAs. In theory, all mappings should have the same decoding errors, given AoA estimation errors of the radar. However, we find that taking the geometric relations of reflection angles into consideration can greatly improve the robustness of METASIGHT. In particular, practical objects may be in located a transition region between two discretized reflection angles. In addition, most objects are not single-point scatterers. Their cross-sections may span multiple angles. So angle sensing becomes a continuous, rather than discrete, problem.

To illustrate the effect of this problem, consider the case where we use 3 metasurfaces to encode reflection angles. The angle bins at 5°, 10°, and 25° are encoded as "011" (*i.e.*, metasurfaces 2 and 3), "100", and "111", respectively. If there is an object at 7.5°, i.e., the boundary of the first two angle bins, all three metasurfaces will reflect signals back to the radar. The radar then detects the codeword "111" and decodes it as 25°, resulting in a significant error.

Objects (Angular Width)	Robust Encoding	Random Encoding
Point Scatter (0°)	2.6°	2.9°
Pedestrian (2°)	2.7°	7.3°
Sphere (10°)	2.9°	8.5°
Surface Alignment Errors	**Robust Encoding**	**Random Encoding**
0.5°	2.6°	6.9°
1°	3.2°	7.6°
1.5°	3.9°	8.9°
3°	9.2°	15.7°

Table 1: Comparison of 90% angle errors of the robust encoding and random encoding.

The fundamental problem of this sort of random encoding method is that even a single error in determining activated metasurfaces may dramatically change the decoded result. We thus propose a *robust angular encoding scheme* to address this limitation. Ideally, we want the codewords of two adjacent angles to differ by at most one bit, which leads to an angle error of at most $\Delta\theta$. In the scenario outlined above, such an encoding technique would select codewords such as "011" and "010" for the adjacent angles 5° and 10°. Then the decoded angle for 7.5° would be either 5° or 10°, resulting in a minimal angle error.

To select such a set of codewords, we leverage a variant of binary reflected Gray codes, which may be efficiently generated through a greedy algorithm [55]. We begin by generating an N-bit binary Gray code with $N = \lfloor \log_2 |\Theta_{RA} + 1| \rfloor$. We then remove the all-zero codeword from the code, and truncate the code to the desired number of encoded angles.

To demonstrate the advantages of the robust angular encoding scheme, we simulate an encoder with a 5° beamwidth and a set of 31 target angles with $\Delta\theta_{RA} = 5°$, and assume the radar SNR is 10 dB. We compare against a baseline method where the codewords are assigned as a monotonically increasing binary sequence. Fig. 4 shows the CDF of the decoded angle error over the designed FoV. Our robust encoding method has an average (95-percentile) angle error of 1.1° (2.1°), much lower than the baseline's angle error of 2.1° (7.9°). The error below the 50$^{\text{th}}$ percentile is due to the resolution limits of the surface, rather than encoding errors.

Table 1 further compares the two encoding methods over various impairment scenarios: *(i) Different types of target objects.* Our robust encoding has a greater benefit compared to the sequential method as the angular width of the target object increases. *(ii) Imperfect deployment.* Installation or manufacturing errors may cause the individual metasurface beams to be misaligned with each other, potentially leading to multiple bit errors. To evaluate such impact, we introduce random sets of alignment errors of varying standard deviations (bottom part of Table 1). We find that even minor errors in metasurface alignment, on the order of 0.5°, more than double the encoding error when using the sequential binar encoding. Our robust encoding method substantially mitigates the effect, until the standard deviation of error increases beyond half of the design beamwidth of the surfaces. At this point, the radar return begins to entirely overlap adjacent beams, and partially overlap non-adjacent beams, causing rapid increases in the resulting encoding error.

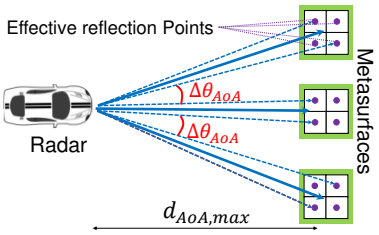

Figure 5: Layout of the Metasight metasurfaces.

3.3 Layout of the Metasurface Reflectors

Finally, we determine the relative physical locations of the metasurfaces. The main requirement is that the radar can resolve reflections from different metasurfaces (*i.e.*, differentiating the AoAs). We denote $d_{AoA,max}$ as the maximum distance for the radar to detect the metasurfaces, which is determined by the desired sensor region (Fig. 1). Given the radar's AoA resolution $\Delta\theta_{AoA}$, *the closest spacing between metasurfaces* for the radar to resolve them separately is approximately $d_{AoA,max} \tan \Delta\theta_{AoA}$, as shown in Fig. 5.

It is worth noting that we cannot simply define the spacing of the metasurfaces as between the center points of the two adjacent metasurfaces. A metasurface that can generate multiple beams does not function as a single-point reflector. Specifically, the *effective reflection points* of different reflection angles do not necessarily overlap at the center of the metasurface. Instead, as shown in Fig. 5, a Metasight metasurface is divided into non-overlapping rectangular subareas, each of which creates a single beam to one of the reflection angles covered by this metasurface. The effective reflection point for each beam is defined as the center of the corresponding subarea. Therefore, we first profile the metasurface at design time and map out the effective reflection points corresponding to different angles. Then we separate adjacent metasurfaces so that the spacing between any pair of their effective reflection points is larger than the radar's angular resolution $\Delta\theta_{AoA}$ (Fig. 5).

4 METASURFACE DESIGN

3D printing techniques are economical and fast solutions for metasurface fabrication. A recent work, MilliMirror [29], proposes a 3D-printed metasurface that can reflect and reshape mmWave signals for communication coverage expansion. A MilliMirror metasurface consists of many unit cells. Each unit cell is a 3D-printed dielectric cuboid whose height can modulate the phase shift of incidental signals. The entire MilliMirror metasurface has a flat dielectric side, exposed to incoming signals, and one "bumpy" side coated with copper. However, the copper coating entails a sophisticated electrodeposition process, *i.e.*, it first deposits an initial layer using sputtering and then thickens the copper using chemical electroplating.

In Metasight, we innovate the metasurface structure to eliminate the complex metal coating process. Besides, the new metasurface structure is more robust to fabrication errors and generates reflection beams with higher gain. Thus, it is more suitable for sensing, which is more sensitive to beam qualities than communication.

4.1 Unit Cell Model

Similar to MilliMirror, the Metasight metasurface consists of 3D-printed dielectric cuboids which function as unit-cell phase shifters.

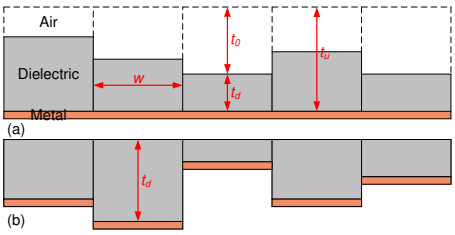

Figure 6: Vertical cross-section of the metasurface structure in (a) METASIGHT, and (b) MilliMirror [29]. Only 5 cuboid unit cells are shown for each metasurface design.

However, the difference is that its conductive reflection layer is flat, *i.e.*, the back sides of all the cuboids share the same surface, allowing us to simply attach the copper tape to replace the copper coating process. The height-varying side of the dielectric faces the incident signals' directions, as illustrated in Fig. 6. To design the 3D-printed dielectric cuboids, we must model the relationship between the dielectric thickness and the associated phase shift. Unlike MilliMirror, signals impinging on the Metasight surface must first go through an air gap with varying heights before entering the cuboids and getting reflected back (Fig. 6). So the unit-cell structure can be modeled as a layer of air, a dielectric layer, followed by a conductive layer. Based on the transmission line model, the input impedance of this stratified structure is [52]:

$$Z_i = jZ_0 \frac{Z_d \tan(k_d t_d) + Z_0 \tan(k_0 t_0)}{Z_0 - Z_d \tan(k_d t_d) \tan(k_0 t_0)} \quad (1)$$

where Z_d, t_d are the characteristic impedance and the thickness of the dielectric layer. And Z_0, t_0 are those of the air layer. k_d and k_0 are the wave number of the signal in the dielectric and the air, respectively. So the reflection coefficient of one unit cell is:

$$\Gamma = \frac{Z_i - Z_0}{Z_i + Z_0} = e^{-j2\arctan\frac{Z_d \tan(k_d t_d) + Z_0 \tan(k_0 t_0)}{Z_0 - Z_d \tan(k_d t_d) \tan(k_0 t_0)}} \quad (2)$$

The phase of the reflection coefficient Γ corresponds to the phase shift generated by the unit cell. Thus, given the thickness $t_u = t_d + t_0$ of a unit cell, the phase shift of the unit cell can be tuned by varying the dielectric thickness t_d. For simplicity of fabrication, the unit-cell cuboids have uniform widths and lengths, denoted as w. We set w to be below $\lambda/4$ over the entire bandwidth of the radar to avoid aliasing. For the 77 GHz automotive radar with 4 GHz bandwidth, the unit cell is approximately 0.9 mm wide.

4.2 Metasurface Structure and Fabrication

According to the Metasight coding scheme (§ 3), a metasurface needs to create multiple reflection beams to cover multiple reflection angles. To achieve it, we divide the metasurface into several non-overlapping rectangular subareas, each of which is responsible for a single beam. For each subarea, we first generate the objective beam pattern, given the beamforming direction and beam width. Then, we search for the optimal dielectric thicknesses of unit cells that minimize the discrepancy between the synthesized and the objective beam patterns, as in [29]. Finally, we combine the unit cells of all subareas to obtain the structure of the metasurface.

The Metasight metasurface has two key advantages compared with MilliMirror. First, Metasight has a slower phase change with respect to the dielectric thickness than MilliMirror, as shown in

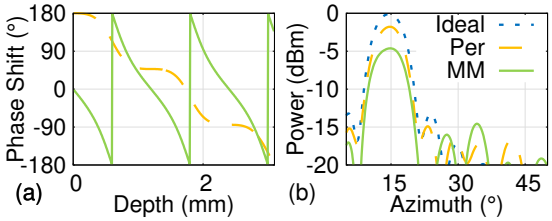

Figure 7: (a) Comparison of the mapping from dielectric depth to phase shift between Millimirror and Metasight. (b) An example of the differing effect of 3D printing errors on the resulting beam pattern for each fabrication process.

Fig. 7a. This is mainly because the phase change of the air layer partially cancels out that of the dielectric layer. The slower phase change means that Metasight is more robust to the printing uncertainty of 3D printers. To demonstrate the benefit, we simulate the beam patterns of Metasight and MilliMirror samples with randomly generated fabrication errors, as shown in Fig. 7b. We find a slight increase in sidelobe levels and a 1.7 dB and 4.5 dB reduction in main lobe levels for the METASIGHT and Millimirror samples, respectively. With a 2.8 dB improvement in main lobe levels, Metasight needs 27.6% less surface area to achieve the same beamforming gain as MilliMirror. Despite thicker dielectric cubes to achieve a phase shift of 2π, Metasight can save material compared to MilliMirror, especially when the surface becomes larger.

Second, with a flat conductive layer, Metasight is much easier to fabricate than MilliMirror. Fig. 8 illustrates a sample of Metasight and a replica of MilliMirror, respectively. Specifically, MilliMirror uses electroplating and sputtering to coat the rugged metal layer, both of which require highly specialized equipment and a laborious process. Moreover, the copper layer must be properly sealed from the outside environment to prevent oxidation and corrosion. In contrast, Metasight only needs a piece of conductive tape whose thickness is larger than the skin depth of the signal, *i.e.*, $<$ 300 nm at 77 GHz. Compared with the metal coating, the conductive tape is easy to manipulate, can be attached tightly to the dielectric layer, and is stable against oxidization.

4.3 Dimensioning of the Metasurface

Detection range. The Metasight metasurfaces reflect the radar signal to the NLoS target object and then relay the target's reflection back to the radar. Using the well-known power budget model, the received power P_r, at the radar is:

$$P_r = \frac{P_t G_t G_r \lambda^2 \sigma_m^2 \sigma_o}{(4\pi)^5 d_r d_o^4}, \tag{3}$$

where P_t is the transmit power. G_t and G_r are the transmit and receive antenna gains. λ is the signal wavelength. d_r is the distance between the metasurface and the radar, and d_o is that between the metasurface and the target object. σ_m is the bistatic radar cross section (RCS) of the metasurface, and σ_o is the monostatic RCS of the target object. RCS is an intrinsic parameter of an object, which measures its ability to reflect incident signals back to the radar.

According to Eq. (3), we can determine the RCS requirement of Metasight, σ_m, given the radar hardware configurations (*i.e.*, P_t, minimum P_r, G_t, G_r), the target characteristics (*i.e.*, σ_o), and the maximum detection distances. The radar configuration is known from its hardware specification. So we need to characterize the scattering

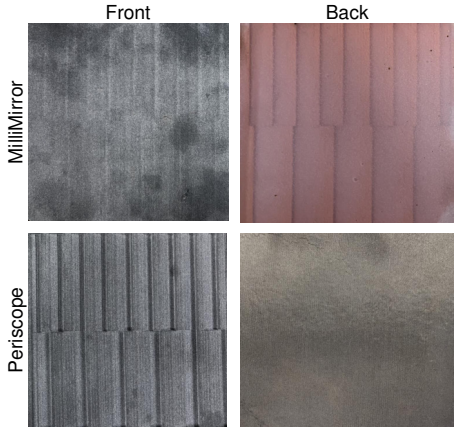

Figure 8: Comparison of Metasight and Millimirror [29] metasurface designs. The *front* photos show the side exposed to the incident and reflected radio waves. The *back* photos show the conductive side of each metasurface.

properties of common objects, such as vehicles and pedestrians, on the road. For object detection and localization, the target object is usually abstracted as a scattering point, whose RCS generally varies with the incident angle. The RCS of the metasurfaces, σ_m, must allow for the detection of the object even with its minimum RCS. Determining the minimum RCS of objects requires empirical RCS measurements, such as those conducted in [9, 21, 33]. We augment these published measurements with our own measurements using the radar configuration described in § 6. Fig. 9 shows that vehicles have much larger RCS than pedestrians. So, in order to detect both pedestrians and vehicles, at least 95% of the time, the RCS threshold of objects is -9 dBsm (5% RCS of pedestrian max point). In addition, to sense the object with more details, such as object orientation and size, vehicle radars need to sense more scattering points from different parts of an object. For example, a vehicle may have scattering points associated with wheel wells, mirrors, and bumper corners [28, 31]. We further calculate the RCS of the second strongest point of vehicles, as shown in Fig. 9. The RCS threshold for detecting at least two scattering points of a vehicle is -19 dBsm.

Given the minimum RCS of the target objects, we can determine the RCS requirement of Metasight. This RCS requirement can be further translated to the size requirement of the Metasight metasurfaces. Given a flat surface with a fixed area A, the maximum RCS is achieved when the surface is metallic and the signal incidents at the broadside direction. In such case, the signal is fully reflected and, just like an ordinary flat panel, the RCS of the surface is [49]:

$$\sigma_m = \frac{4\pi A^2}{\lambda^2}. \tag{4}$$

In practice, a Metasight metasurface can only reflect the signal with an efficiency of $\eta < 1$ due to the existence of the sidelobes. Thus, the required minimum area of the Metasight metasurface is $A = \lambda\sqrt{\frac{\sigma_m}{4\pi\eta}}$. η can be calculated as the ratio between the main lobe level and the sum of all side lobe levels of the metasurface's beam pattern. The total size of each metasurface will be the required per-beam area A multiplied by the number of beams per surface.

Beam squint effect. The model of unit cells assumes a single frequency, based on which the dielectric thickness of the unit cells

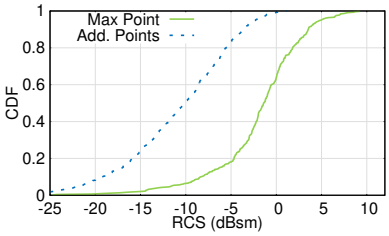

Figure 9: Statistics of RCS of vehicles and pedestrians.

is calculated. Thus, the metasurface experiences beam distortions with the actual wideband radar signal. To avoid significant effects, theoretical guidelines [29] dictate that we should design a surface where

$$Bd \leq \frac{c}{|\cos\gamma_i + \cos\gamma_r|}, \tag{5}$$

where B is the radar signal bandwidth, d is the maximum dimension of the beamformer, and θ_i and θ_r are the angles between the maximum dimension of the surface and the incidence and reflected vectors, respectively. Given the 4 GHz maximum bandwidth available, beam squint will not have an effect so long as each beamforming metasurface has a maximum dimension of 15 cm or less.

4.4 Fabrication Errors

During fabrication, we note that there are two key sources of error: *printing uncertainty*, which occurs due to inaccurate positioning of the printer head and amount of material deposited, and *warping*, which occurs due to uneven cooling of the 3D-printed object after printing is complete. Printing error is generally well-specified by the manufacturer of the 3D printing process. For example, our 3D printing process has an expected accuracy of ± 0.2 mm $\pm 0.005l$, where l is the maximum length of the dimension of interest [16]. As discussed in Sec. 4.2, Metasight is more robust to printing uncertainty than MilliMirror [29], thanks to the slow phase change with respect to the dielectric thickness.

Warping is difficult to model analytically, but we observe that it is more severe in flexible and thin 3D printed metasurfaces like Metasight. Therefore, to reduce the effect of warping, we make the metasurface more rigid by adding a small, 5 mm wide and 5 mm thick border around the edges of the dielectric surface. This border has a relatively small area. For example, on a 12 cm $\times$ 13 cm surface, the border region is only 25 cm^2. Based on Eq. 4, the RCS of the border region is 16 dB lower than that of the beamforming region. So it will have a negligible impact on the desired beamforming patterns.

5 ROBUST DECODING OF NLOS ANGLES

NLoS sensing with Metasight requires correct angle coding, which in turn relies on accurate beamforming. However, we find that the theoretical beamforming patterns suffer from distortions in practice. Thus, we develop a robust decoding process to overcome them.

5.1 Decoding in Environmental Dynamics

The standard signal processing of automotive radars consists of three steps. First, it generates a 2D heatmap along two axes, *i.e.*, range and Doppler shift. Second, it uses a 2D constant false alarm rate (CFAR) detector to detect objects in the heatmap. Finally, for each detected object, it combines measurements from all receiving antennas to estimate the AoA of the object. Metasight only maps the reflection angles to the AoA patterns observed by the radar, so it does not need to change the first two steps. However, three challenges remain due to environmental dynamics in practical scenarios: *(i)* paths from multiple metasurfaces may fall into the same range and Doppler bin, necessitating algorithms to resolve multiple AoAs; *(ii)* paths from different metasurfaces to an object may have slightly different range/Doppler values, and *(3)* reflections do not occur at a fixed point on a metasurface (Sec. 3.3), so the metasurface's azimuth from the radar's perspective may vary.

For the first case, we must resolve an arbitrary number of closely spaced AoAs with the same range and Doppler shift values. Specifically, our signal processing algorithm needs to distinguish the weak signal of one AoA from the side lobes of the strong signal of another AoA. To this end, we adapt the Fast Iterative Interpolated Beamforming (FIIB) algorithm [1], which efficiently estimates multiple AoAs by successively canceling the sidelobes of each estimated AoA, and then iteratively refining each AoA. However, we lack *a priori* knowledge of the number of AoAs, which is needed in FIIB [1]. To work around this limitation, we add a stopping condition at the end of each FIIB iteration, *i.e.*, the algorithm stops attempting to estimate additional AoAs if either the number of AoAs exceeds the number of metasurfaces, or if the magnitudes of the AoAs falls below a noise threshold N_0. N_0 is determined by applying a CFAR threshold, based on the remaining AoA spectrum power after the current AoA is subtracted. If the current AoA falls below the false alarm threshold, where the noise term is the average power of the remaining angular spectrum, the current AoA is dropped, and no further AoAs are estimated.

The second challenge occurs when slight differences in the paths from the radar to each metasurface to the occluded point result in slightly differing range and Doppler values. If we do not properly combine the signals from all these paths, we cannot correctly decode the reflection angle. The difference in range between any two metasurface reflectors is approximately

$$\Delta R \approx \Delta x\,(\sin\theta_i + \sin\theta_r)\,, \tag{6}$$

where Δx is the spacing between the two metasurfaces, and θ_i and θ_r are the incident (radar to reflector) and reflected (reflector to object) angles. Intuitively, the range difference is contributed by the propagation delays of both the incident signal and reflection signal, *i.e.*, $\Delta x \sin\theta_i$ and $\Delta x \sin\theta_i$ The variation in observed velocity is

$$\Delta v \approx v_{\parallel} \frac{\Delta x \cos\theta_r}{R_o}, \tag{7}$$

where $v_{\parallel}$ is the tangential velocity of the object with respect to the metasurfaces and R_o is the distance between the object and the metasurfaces. Intuitively, the velocity difference is due to the slightly different reflection angles of different metasurfaces. For example, for a three-surface reflecting structure with a 30° FoV, located up to 10 m from radar with a 2° angular resolution, the maximum Δx is 70 cm and the maximum range variation is 35 cm. For an occluded vehicle traveling at 25 mph (40 km/h) at a range of 2 m or greater from the surface, the variation in observed velocity may be up to 9 mph (14 km/h). Conversely, for the very small incident and reflected angles, the range variation may be less than 2 cm. Since the 77 GHz automotive radars can have a range resolution of 5 cm and velocity

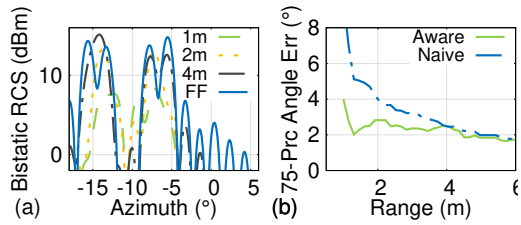

Figure 10: Illustration of *encoding near-field* effect. (a) The decoded angle errors at different distances of the near-field aware decoding and the default decoding. (b) The near-field effect on the effective beam pattern of a metasurface.

resolution of less than 1 km/h, we must consider both scenarios where all paths fall in the same range and Doppler bin, as well as in diverse bins. To handle both scenarios, after completing the initial FIIB AoA estimation stage, we merge the estimated AoAs of multiple adjacent range and angle bins into a single set of AoAs using hierarchical clustering.

To handle the variation in possible reflection points on the metasurfaces, rather than probing a single azimuth angle to detect if a metasurface has an active reflection, we determine a range of possible azimuth angles where the reflecting point may be located. To calculate this azimuth range, we begin by determining the effective reflection points of each metasurface. Since each metasurface consists of a set of discrete beamforming subareas, the effective reflection point is ideally located at the center of each subarea (Sec. 4.3). We then determine the allowable azimuth range for each metasurface by mapping each subarea to an azimuth angle, based on our prior knowledge of the metasurface location. The azimuth range between the minimum and maximum scattering angles is designated as the allowable azimuth range. We demonstrate the validity of this technique in § 6.3.

5.2 Near-Field Aware Decoding

The pattern synthesis of Metasight assumes that both the target and the radar are in the far-field region of the reflector to accurately map the LoS AoAs to reflection angles. However, the far-field assumption no longer holds if either the target or the radar is in the near-field of the metasurface, which causes non-negligible distortions.

The theoretical boundary between the near-field and far-field regions is approximated as $2D^2/\lambda$, where D is the maximum side length of the reflector, and λ is the radar signal wavelength [35]. But fortunately, even within the theoretical near-field region, the effective beam pattern bears similarities to the designed far-field pattern. Fig. 10(a) illustrates this effect on a surface designed to beamform to $-5°$, $-8°$, $-13°$, and $-16°$. The surface is 12 cm wide and has a far-field boundary of 7.6 m at 79 GHz. Notice that the near-field patterns do share similarities with the far-field, with two key differences: the main lobes are shifted, and the magnitude of the main lobes is slightly lower. Also, notice that the main lobes do not significantly deviate from the far-field patterns until a distance of less than 4 m, which is significantly shorter than the theoretical far-field distance. Below this distance, both the center of the beams shift and the widths of each beam may change. While a simple reduction in beam power in the near field may be offset by reduced path loss, distortions in beam width and direction are likely to result in

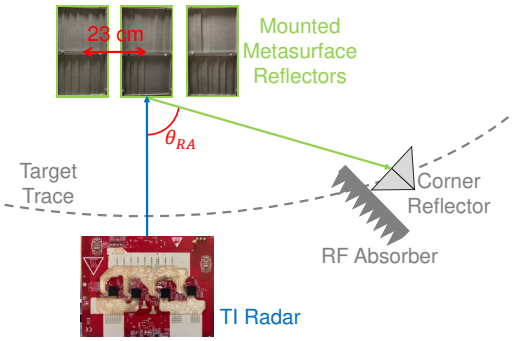

Figure 11: Experimental setup for evaluating the NLoS FoV and angle decoding accuracy.

errors in the decoding of the reflection angle. Just as beamforming near-field distortions arise from the assumption that the incident signal to a metasurface is a plane wave, an *encoding near-field distortion* arises because we assume the incident signal across the entire metasurface array is a plane wave, such that the AoA of the signal at each metasurface is the same. However, this is clearly not the case when the occluded object or the radar is near the metasurface array. In fact, since the metasurfaces must be separated by enough distance for the radar to separately resolve each by their differing azimuth angles, the AoA at each surface must differ by at least the radar angular resolution $\Delta\theta_{AoA}$ to decode the reflection angle θ_{RA}.

To correct the near-field distortion, we build a *near-field aware reflection angle decoder*, which explicitly remaps the codeword for near-field cases. Specifically, first, we simulate the distorted AoA spectrum at each near-field distance D and reflection angle θ_{RA}. Then, we find the codeword for each distance and angle combination using the decoding method described above. Finally, we aggregate the reflection angles with the same codewords by selecting the median one as the target reflection angle, which minimizes the angle estimation error. In practice, when the radar detects an occluded object in the near-field region, it uses the distance to the metasurfaces D to retrieve the codewords for different reflection angles. It then finds the codeword closest to the decoded one and uses the corresponding reflection angle $\theta_{RA,opt}$ as the decoding result. In Fig. 10(b), we simulate this method with a set of four metasurfaces with a reflection angle resolution of $2°$. We find that our method can reduce the angle estimation error by more than 50%.

6 EVALUATION

To evaluate Metasight, we fabricate three metasurface panels to cover seven NLoS reflection angles with a spacing of $4°$, and thus a total azimuth range of $24°$ from the minimum to the maximum encoded angle. Each metasurface consists of around 38k unit-cell elements and has a size of $13 \times 24\text{cm}^2$. Each metasurface reflects signals to 4 separate angles, with each beamforming subarea being 6.5×12 cm^2, and the subareas arranged in two rows and two columns. We mount the metasurfaces at the minimum spacing allowable for their distance from the radar (§ 3.3), 23 cm when the radar is 4 m from the reflectors. The reflectors occupy a total width of 60 cm. The total cost of fabrication was only \$77 per surface, which is within the range of ordinary costs for installing a standard traffic sign [50], and can be reduced at larger production volumes.

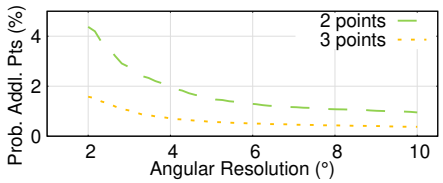

Figure 12: Empirical probability of more than 2 or 3 angle values corresponding to a single range/doppler bin.

Our experiments use a TI cascaded automotive radar operating in the 76-81 GHz band [17]. We configure the radar with a distance resolution of 6 cm and a maximum unambiguous distance of 15 m. By using the entire MIMO antenna array, the radar can achieve an angular resolution of up to 1.4°. The radar streams its raw I/Q samples to a PC host, where the robust NLoS angle decoding workflow (Sec. 5) is implemented in Matlab.

To evaluate the performance of Metasight with static scatterers, we use a trihedral corner reflector with 20 cm side length as the object. We block the LoS path from the radar to the corner reflector using an RF absorber, and incrementally move the corner reflector to each angle, as illustrated in Fig. 11. We conduct this experiment in an empty field to minimize static clutter which could hide the static targets. Practical targets are generally moving, and are separated from clutter using their doppler shift, as demonstrated in § 7.3.

6.1 Microbenchmark: Radar Point Sparsity

We first validate the angle sparsity assumption (§ 3.1) by collecting 8 minutes of LoS radar data from a busy road intersection. We then use the constant false alarm rate (CFAR) to detect all points corresponding to moving objects, totaling over 100,000 detected points. We evaluate the number of points detected, and find that there is a 4.4% chance of at least 1 conflicting angle with a 2° metasurface angular resolution and a 1.5% chance with a 5° resolution. Where multiple conflicting angles are present, our dense angular encoding may cause errors in position estimation. Since this conflict rate is close to the expected false alarm rate of CFAR, we conclude that any resulting errors may be handled using the same methods used to handle false alarms in standard LoS radar signal processing.

6.2 Microbenchmark: Reflection beam pattern

Fig. 13 shows the measured beam patterns from one of the metasurfaces. For comparison, we fabricate a MilliMirror surface [29] with the same configuration. We verify the Metasight metasurface generates the reflected beams at desired angles. The beamforming accuracy is similar to MilliMirror, despite its significantly simplified fabrication process. We find that our metasurface design has a loss of only 2 dB compared to an ideal surface, and a 1 dB improvement compared to MilliMirror, due to its improved error tolerance.

6.3 Microbenchmark: Reflection Point Variation

As discussed in § 5, to ensure that the radar can independently resolve each metasurface, we must account for variation in the exact reflection point on each surface. Given that our prototype metasurfaces are designed with 6.5×12 cm beamforming regions, we expect the reflection points to be about 6.5 cm apart. We determine the actual distance between the reflection points by measuring the range

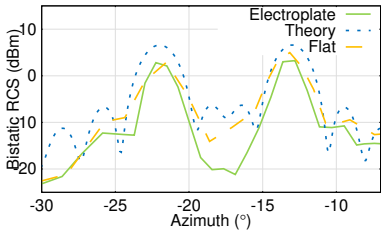

Figure 13: Fabricated metasurface beam patterns. "Flat": Metasight; "Electroplate": MilliMirror; "Theory": Ideal.

to the reflecting surfaces and the angle between them. We find that the reflecting points may be found up to 7 cm apart, within only about 5 mm deviation from the theoretical separation.

6.4 Microbenchmark: Interference from Mounting Structure

To ensure that each metasurface reflector is precisely aligned to point in the same direction and correctly spaced, we attach them to a rigid mounting structure, consisting of a set of small brackets with the minimal cross-sectional area. Before proceeding with our primary tests, we investigate whether NLoS reflections from the metasurface mounting structures will interfere with reading NLoS reflections from the metasurfaces themselves. We place the corner reflector at multiple angles within the FoV of our metasurfaces, and conduct measurements with and without the metasurfaces attached to the mounting structure. The radar returns from the metasurface NLoS reflections are an average of 18 dB higher than NLoS reflections from the mounting structure. This is well below the decoding noise floor threshold, implying that the mounting structure is unlikely to impact angle decoding.

6.5 Microbenchmark: Sensing Range

We verify that we can correctly select the RCS requirements of the metasurfaces by measuring the pedestrian sensing range of a set of test metasurfaces. We fabricate three metasurfaces with beams at 13° and 16° angles. The metasurfaces have three different sizes: 4.5×4.5 cm^2, 9×9 cm^2, and 15×15 cm^2, with half of the surface allocated to each beam, corresponding to per-beam RCS values of -0.5 dBsm, 12 dBsm, and 20 dBsm, respectively, following the model in § 4.3. We configure the radar for a maximum unambiguous range of 30 m, and a range resolution of 12 cm. Then, we place the metasurface in front of the radar, while a pedestrian moves within the target beamforming region and gradually increases the distance to the metasurface. We record the maximum distance at which the pedestrian remains detectable above the noise floor at a 1% false detection rate, and compare it to the theoretical detection range model developed in § 4.3. We find that the actual detection ranges fall within the predicted range (Table 2), showing that our model can accurately determine the required metasurface size in this manner.

6.6 Microbenchmark: Height Mismatch Between Radar and Reflector

To understand the effect of the vertical placement of reflectors, we mount the radar at a height of 1 m, and place a single 15×15 cm metasurface reflector at a distance of 1.8 m from the radar. Then, a

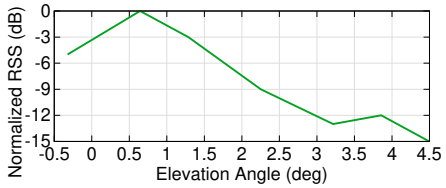

Figure 14: Effect of radar/metasurface height mismatch

Surface Size	Measured Range	Theory Range
4.5×4.5cm	8m	8-14m
9×9cm	17m	13-20m
15×15cm	24m	17-25m

Table 2: Comparison of measured pedestrian detection range to theoretical detection range based on metasurface size and empirical pedestrian RCS measurements.

1.8 m tall pedestrian moves within the reflector's coverage region at a range of 5-10m from the radar. We vary the height of the reflector and measure the received signal strength from the moving pedestrian, normalized by the free-space path loss to the pedestrian's location. Figure 14 shows the signal strength as a function of the elevation angle from the radar to the reflector. We find that the signal strength rapidly drops as the metasurface deviates from its optimal height.

In practical deployments, the height of the radar will vary between different vehicles, making it effectively impossible to precisely match the height of the reflector to the height of the radar. To work around this problem, we suggest increasing the height of each reflector, such that it can match any given vehicle bumper height. Given that common car bumper heights range from approximately 35–80 cm [4], a metasurface reflector with a height of 0.6m or less can be reasonably expected to cover the range of radar locations.

6.7 Comparison to Natural Reflectors

We now demonstrate the advantages of our Metasight design over natural reflectors that do not leverage angular encoding. First, we compare the Metasight reflector to two common reflectors found in a natural environment: a convex metal reflector and a planar metal reflector. We select the natural reflectors and metasurface spacing (23 cm) such that each reflector has the same total width. Each reflector type is placed at the same location 4 m from the radar. We follow the point scatterer measurement procedure described above and sweep through the entire FoV of each reflector, at a range of 6 m from the reflector structure. The FoV of each reflector is defined as the range of angles where the NLoS path from the reflector exceeds the noise/clutter floor. To ensure we measure the upper performance bound of the conventional reflectors, we obtain the position, angle, and shape parameters of these reflectors by fitting the reflector model to the collected radar data. Therefore, practical performance is likely to be worse, since there is an additional error introduced in the process of localizing and characterizing the reflectors. For example, a 0.1° error in localizing the azimuth angle of the cylinder with respect to the radar would result in a 3-6° error in the reflection angle estimate. For evaluation, we localize the metasurfaces to within 1°, and decode the angles following the process in § 5.

Our experimental results, shown in Table 3, demonstrate that METASIGHT achieves a more than 3× larger FoV than a planar reflector, with only about 25% higher average angle error, while taking up the same amount of space. It also achieves an over 5× improvement in worst-case angle error over the idealized convex reflector, while an ideally-shaped conventional reflector without our efficient encoding scheme would need to be at least 1.4 m wide, more than double of the total width span of the Metasight reflectors.

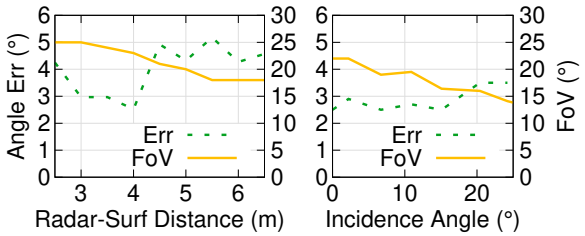

Figure 15: Effect of sensor movement on angle error and FoV.

	FoV	Mean Err	95% Err	Loc Err
Planar reflector	8°	2.0°	3.4°	21 cm
Convex reflector	100°	10°	26°	104 cm
METASIGHT	24°	2.5°	4.75°	27 cm

Table 3: Comparison of FoV, angular error, and localization error between natural NLoS reflectors and Metasight.

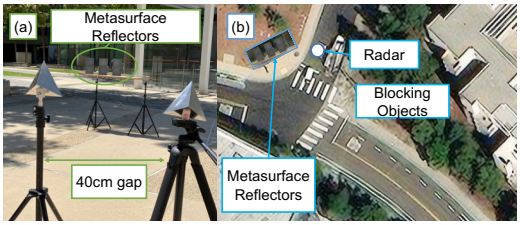

Figure 16: Experimental setup for (a) the multi-object case study and (b) the roadside detection case study.

An essential factor limiting the angle accuracy is the beam width, which is inversely proportional to the metasurface size. Thus, to achieve higher angle accuracy, larger metasurfaces are needed. In addition, narrower beams increase the near-field range of Metasight, which must be addressed using the near-field aware coding in Sec. 5.2.

6.8 Radar Mobility

Metasight assumes that the location of the metasurfaces are quasi-static within a radar sensing frame. This is reasonable because the radar frame lasts for less than 5 ms, equivalent to less than 15 cm of movement at even highway speeds. To understand the effect of radar movement on the angle sensing accuracy and field of view (FoV), we repeat the procedure in § 6.7, moving the radar 50 cm between measurements, equivalent to 22 mph (36 kmh) with a 20 Hz frame rate. The results (Fig. 15) show that optimal accuracy is achieved at the designed sensing range of 4 m. Accuracy is reduced by up to 50% at longer ranges (where the radar cannot reliably resolve individual reflectors) and very short ranges (due to the near-field effect). This optimal range may be increased trivially by increasing the spacing between the metasurfaces. The FoV decreases slightly at longer ranges due to the reduction in near-field effects. We also vary the incidence angle of the radar with respect to the metasurfaces, and find that the performance of the system does not significantly degrade within 15° of the design location of the radar. With larger incidence angle variations, reflection angles become misaligned, leading to reduced accuracy and FoV.

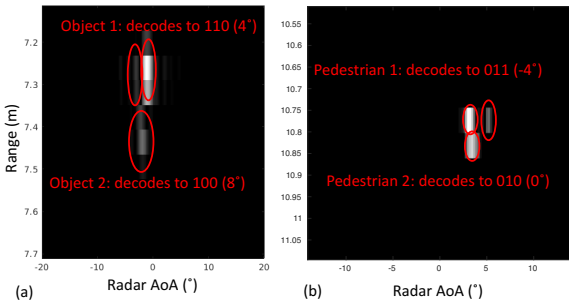

Figure 17: (a) Radar heatmap image of the encoded locations of two adjacent point scatterers and (b) pedestrians.

7 CASE STUDIES

7.1 Resolving Multiple Objects

One of the major benefits of Metasight over existing NLoS radar sensing [48, 56] is that our method can achieve high angle resolution and effectively localize multiple closely-spaced points. To demonstrate this ability, we use two adjacent corner reflectors as occluded target objects. We place them in adjacent beamforming regions, and gradually move them apart until the radar can resolve them separately. Note that although the radar range resolution is 6 cm, the NLoS sensing resolution is limited by the range-variation effect described in § 5. We find that the radar can separately resolve these objects when they are at least 35 cm apart, equal to the range spread we estimated using Eq. 6. The corresponding radar range/angle heatmap is displayed in Fig. 17a. The experiment also verifies that the reflection angle is decoded correctly, to 4° and 8°, at the designed resolution of 4°. We repeat this for two pedestrians walking away from the surfaces at constant angles relative to the metasurfaces at a range of 5-9 m from the metasurfaces. We find that the minimum separation distance is slightly higher, 70 cm, since pedestrians are not point scatterers (Fig. 17b).

7.2 Separating NLoS and LoS Paths

Next, we demonstrate that Metasight can separate the NLoS paths from objects moving in the LoS region behind the reflectors and those NLoS paths caused by ambient reflectors. In this experiment, a pedestrian walks past the metasurfaces at a range of 6 m across a distance of 3 m (the FoV of the surfaces) for 100 s, in both the NLoS and LoS regions. We find that the pedestrian is incorrectly detected by Metasight only 1.9 % of the time in the LoS region, when the pedestrian overlaps the sensing region of one of the metasurfaces.

7.3 Sensing Road Users

Finally, we demonstrate our system for sensing occluded objects in real-world transportation environment. We place the radar behind a concrete wall that blocks the view of a crossroad, and place the three-metasurface reflectors 4 m away, in a location with a view of both the radar and the occluded portion of the road (see Fig. 16b). This road has sidewalks, two vehicle lanes, and bike lanes. We then collect data as pedestrians, bicycles, and motor vehicles move within this occluded region. We find that we can detect moving pedestrians at ranges of 20 m or more, as well as vehicles at ranges of up to 28 m. We plot a number of of NLoS traces, overlaid over a diagram

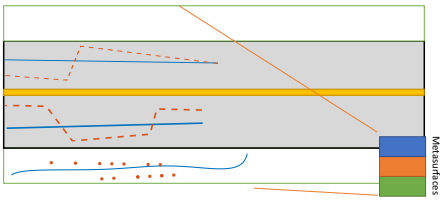

Figure 18: Measured roadside trajectories of vehicles (dashed line) and pedestrian (points) alongside lidar-measured ground truth (solid line).

of the road in Fig. 18. By examining the traces, we find that we can determine the lane position of an occluded vehicle to within 1.2 m of its true position, sufficient to determine its current lane. We further determine that pedestrians are localized with an RMSE of 0.7 m.

8 RELATED WORK

NLOS radar sensing. Prior work on NLoS radar has explored various reflectors in the environment to localize obstructed objects. For example, Scheiner *et al.* [32] proposes first to use lidar to identify planar reflectors such as walls, and then use a geometrical ray-tracing model to map the reflected radar signal features to the location of an NLoS object in an urban environment. Similar approaches are adopted by [13, 40, 41]. As mentioned in Sec. 2, such methods need an excessively large reflector to achieve acceptable coverage. Other works [48, 56] propose to harness multiple natural or artificial reflectors to triangular the objects, yet a sufficient number of reflectors (*e.g.*, 6 in [48]) with large separation is needed, all within the LoS of the radar, which may not be feasible in practice. CornerRadar [61] introduces a data-driven ray-tracing method for NLoS localization in more sophisticated indoor environments, where signals can experience higher-order reflections and even penetrate obstructions. The machine learning model of CornerRadar requires an accurate 3D map of the environment as input, which may not be available in practice. NLoS radar sensing is also related to the vast literature on device-free indoor localization (see [24] for a comprehensive survey). Yet this line of work mostly assumes a LoS path is always available and aims to disentangle the NLoS paths from it through time-of-flight, AoA, or trilateration. Techniques similar to through-wall radar sensing or imaging [3, 27, 36, 53] are also unsuitable for transportation settings, where occlusions are commonly made of metal or concrete, thus introducing too much attenuation to allow for radar sensors to detect objects behind them.

Metasurfaces for wireless sensing. Prior work has proposed both active [30, 38, 59] and passive [25, 60] metasurfaces for sensing applications. Metasight departs from this literature in two key ways: *first*, in most prior work, the metasurface is directly attached to the transceiver, within its near field. They are intended as an inexpensive way to improve its angular resolution compared to MIMO arrays or phased arrays. By contrast, our system is designed for placement in the environment and improves resolution by moving angular beamforming closer to the target of interest. *Second*, prior work uses either active time-based beam scanning [59] or passive frequency-based beam scanning [6, 60] to scan multiple angles. Time-based methods change the reflection beam pattern of the metasurface across different radar frames. But it requires active phase shifting or switching elements, which significantly compounds the

cost and complexity of the metasurface, especially at mmWave bands. Frequency-based beam scanning limits the achievable angular field of view and range resolution of the radar, since each angle uses only a limited bandwidth compared to the full bandwidth allocated to the radar.

NLoS sensing through alternative modalities. Prior research in computer vision/graphics explored seeing-around-corner using either active laser illumination or super-resolution cameras. These methods are applicable only in short-range and controlled environments and often require high-cost equipment. NLoS Lidar sensing [7, 8, 19, 26, 51] can achieve high-resolution. But to receive reflections from ordinary reflectors, it requires impractical illumination levels above eye safety limits. Other modalities such as acoustic [2, 18] and thermal infrared [20] sensing also fall short of the range and coverage requirements in practical transportation environments (Sec. 2.1).

NLoS mmWave communication and beam tracking. [57] Similar to mmWave radar sensing, mmWave communication is sensitive to environmental reflections due to the use of highly directional beams. Recent work [54, 57, 62] proposed to map out the environment using mmWave or lidar sensing, followed by a ray-tracing model that guides the beam steering and reduces the probability of blockage. Prior work in mmWave communication has also explored ways to "compress" the beam space to reduce beam management overhead [14, 45, 46]. Our encoding method differs by designing the encoding to account for the angular spread of common objects of interest in sensing scenarios. We also scan the encoded beam information in a different manner – rather than directly scanning the beams, we indirectly scan them using radar.

9 DISCUSSION

Practical deployment of Metasight. Metasight requires fine alignment with the road to accurately map NLoS angles to target locations. To make such alignment easy for non-experts, such as road workers, we can visually mark the edge beam directions of Metasight on the plate that holds all metasurfaces. During the deployment, the road worker first identifies the location of Metasight, and the two edges of the NLoS region, according to the deployment plan and the local map. Then, workers can use a laser-level instrument to align the visual markers of beams to the edges of the NLoS region. A typical long range outdoor laser has an angular error around $1'$, which is sufficient for the alignment of Metasight.

Protection from harsh environment. Metasight is deployed outdoors and hence subject to weather and other adverse conditions, which may over time erode the surface, introduce random phase errors, and reduce the main lobe gain of Metasight. To reduce the impact of this damage, RF-transparent materials such as plastic film can be used to seal the metasurface from the environment with minimal impact on its RF characteristics. To verify the impact of the plastic film, we conduct a simulation by adding PET film with common thickness (i.e., 100 μm) in front of a metasurface. The simulation results show that the film only introduces a 0.2 dB loss. The maximum phase error introduced is only 15°, which is negligible.

Detection of Metasight at intersections. The radar needs to localize Metasight before beamforming toward it. However, since the metasurfaces of Metasight do not have a distinctive radar signature, additional sensors or infrastructure are required for localization. The first solution is using cameras on vehicles. Specifically, we can deploy visual signs around Metasight, which the vehicle camera can detect and localize [10]. The second solution is using lidar coupled with a high-resolution map [11]. Specifically, we deploy Metasight around a road sign, which the lidar can detect. Then, with the high-resolution map, the vehicle can identify the co-located Metasight for NLoS sensing. Alternately, additional RF infrastructure can also be installed for localization purposes, such as passive radar tags [25, 43]. These tags modulate data to their backscattered radar signals, allowing them to be jointly localized and communicated with, allowing Metasight to be detected and localized.

Impact of LoS blockage between radar and metasurfaces. In crowded environments where the paths to ground-level metasurfaces may be blocked, access to NLoS sensing paths may be ensured by either increasing path diversity with additional metasurface locations, or by placing metasurfaces at a higher elevation. Elevated metasurfaces will require main lobes pointed downward to compensate for the change in incident angle elevation, as well as larger dimensions to account for path loss. Leveraging additional NLoS reflections between the radar and metasurfaces is unlikely to be practical due to the increase in reflection loss.

Impact of vehicle engine vibration. Our measurements do not include vehicle engine-induced vibrations. However, the vehicle vibration only introduces noise in the Doppler frequency spectrum [15]. Metasight relies on angle measurements, which are less impacted by vehicle vibration.

Impact of Metasight on communication efficiency. At the design frequency of Metasight (i.e., 77-81 GHz), Metasight functions as an irregularly shaped metal reflector, similar to other reflective objects in the environment, e.g., vehicles. Metasight only creates a moderate channel impact by creating a few multipath. At standard communication frequencies below 30 GHz, Metasight appears more like a diffuse scatter, changing the reflection gain of the signals hitting it by a minor amount.

Generalization to different frequencies. Metasight is designed for the newest generation of automotive radar at 77-81 GHz. However, our NLoS sensing technique is applicable to other frequencies as well, such as 24 GHz for obsolete radars. To apply Metasight to other frequencies, the metasurfaces must be designed to match these frequencies. Specifically, according to Eqn. 3 and 4, a lower frequency requires a larger physical metasurface area for any given desired detection range.

10 CONCLUSION

Through Metasight, we have verified the feasibility of using metasurfaces to enhance NLoS radar sensing. The Metasight metasurfaces are fully passive, and can only map a fixed set of NLoS reflection angles into a compact set of angular signatures on the radar's AoA spectrum. However, by using efficient encoding on the metasurface reflectors and robust decoding algorithms on the radar, Metasight can improve the FoV and angle resolution by multi-folds, and reduce the reflector size by multi-folds compared with state-of-the-art NLoS sensing that employs natural reflectors. Metasight points to an important direction that enhances wireless sensing through passive yet intelligent reflectors.

ACKNOWLEDGMENTS

We appreciate the insightful comments and feedback from the anonymous reviewers and shepherd. The work reported in this paper is supported in part by the NSF under Grants CNS-1901048, CNS-1925767, CNS-2128588, and CNS-2312715.

REFERENCES

[1] Aboutanios, E., Hassanien, A., Amin, M. G., and Zoubir, A. M. Fast iterative interpolated beamforming for accurate single-snapshot doa estimation. *IEEE Geoscience and Remote Sensing Letters 14*, 4 (2017).

[2] An, I., Lee, D., Choi, J.-w., Manocha, D., and Yoon, S.-e. Diffraction-aware sound localization for a non-line-of-sight source. In *2019 International Conference on Robotics and Automation (ICRA)* (2019), IEEE.

[3] Aubry, A., De Maio, A., Foglia, G., and Orlando, D. Diffuse multipath exploitation for adaptive radar detection. *IEEE Transactions on Signal Processing 63*, 5 (2015).

[4] Aylor, D., Ramirez, D. L., Brumbelow, M., and Nolan, J. M. Limitations of current bumper designs and potential improvements. *SAE Transactions 114* (2005).

[5] Bareiss, M., Scanlon, J., Sherony, R., and Gabler, H. C. Crash and injury prevention estimates for intersection driver assistance systems in left turn across path/opposite direction crashes in the United States. *Traffic Injury Prevention* (2019).

[6] Boljanovic, V., Yan, H., Lin, C.-C., Mohapatra, S., Heo, D., Gupta, S., and Cabric, D. Fast beam training with true-time-delay arrays in wideband millimeter-wave systems. *IEEE Transactions on Circuits and Systems I: Regular Papers 68*, 4 (2021).

[7] Caramazza, P., Boccolini, A., Buschek, D., Hullin, M., Higham, C. F., Henderson, R., Murray-Smith, R., and Faccio, D. Neural network identification of people hidden from view with a single-pixel, single-photon detector. *Scientific reports 8*, 1 (2018).

[8] Chan, S., Warburton, R. E., Gariepy, G., Leach, J., and Faccio, D. Non-line-of-sight tracking of people at long range. *Optics express 25*, 9 (2017).

[9] Chen, M., and Chen, C.-C. Rcs patterns of pedestrians at 76-77 ghz. *IEEE Antennas and Propagation Magazine 56*, 4 (2014).

[10] Doval, G. N., Al-Kaff, A., Beltrán, J., Fernández, F. G., and López, G. F. Traffic sign detection and 3d localization via deep convolutional neural networks and stereo vision. In *2019 IEEE Intelligent Transportation Systems Conference (ITSC)* (2019), IEEE, pp. 1411–1416.

[11] Ghallabi, F., El-Haj-Shhade, G., Mittet, M.-A., and Nashashibi, F. Lidar-based road signs detection for vehicle localization in an hd map. In *2019 IEEE Intelligent Vehicles Symposium (IV)* (2019), pp. 1484–1490.

[12] Gros, J.-B., Popov, V., Odit, M. A., Lenets, V., and Lerosey, G. A reconfigurable intelligent surface at mmwave based on a binary phase tunable metasurface. *IEEE Open Journal of the Communications Society* (2021).

[13] Guo, S., Zhao, Q., Cui, G., Li, S., Kong, L., and Yang, X. Behind corner targets location using small aperture millimeter wave radar in nlos urban environment. *IEEE Journal of Selected Topics in Applied Earth Observations and Remote Sensing 13* (2020).

[14] Hassanieh, H., Abari, O., Rodriguez, M., Abdelghany, M., Katabi, D., and Indyk, P. Fast millimeter wave beam alignment. In *Proceedings of the Conference of the ACM Special Interest Group on Data Communication (SIGCOMM)* (2018).

[15] Hau, F., Baumgärtner, F., and Vossiek, M. The degradation of automotive radar sensor signals caused by vehicle vibrations and other nonlinear movements. *Sensors 20*, 21 (2020).

[16] HP. HP 3D HR PA 12 for the HP Jet Fusion 4200 3D printing solution, 2020.

[17] Intruments, T. mmWave cascade imaging radar evaluation module, 2022.

[18] Lindell, D. B., Wetzstein, G., and Koltun, V. Acoustic non-line-of-sight imaging. In *Proceedings of the IEEE/CVF Conference on Computer Vision and Pattern Recognition (CVPR)* (2019).

[19] Lindell, D. B., Wetzstein, G., and O'Toole, M. Wave-based non-line-of-sight imaging using fast f-k migration.

[20] Maeda, T., Wang, Y., Raskar, R., and Kadambi, A. Thermal non-line-of-sight imaging. In *2019 IEEE International Conference on Computational Photography (ICCP)* (2019).

[21] Matsunami, I., Nakamura, R., and Kajiwara, A. Rcs measurements for vehicles and pedestrian at 26 and 79ghz. In *International Conference on Signal Processing and Communication Systems* (2012).

[22] Najm, W., Smith, J., and Yanagisawa, M. Pre-crash scenario typology for crash avoidance research. NHTSA, 2007.

[23] Nayeri, P., Yang, F., and Elsherbeni, A. Z. *Reflectarray antennas: Theory, designs and applications*. Wiley-IEEE Press, 2018.

[24] Ngamakeur, K., Yongchareon, S., Yu, J., and Rehman, S. U. A survey on device-free indoor localization and tracking in the multi-resident environment. *ACM Computing Surveys 53*, 4 (2020).

[25] Nolan, J., Qian, K., and Zhang, X. Ros: Passive smart surface for roadside-to-vehicle communication. In *Proceedings of the ACM SIGCOMM Conference* (2021).

[26] O'Toole, M., Lindell, D. B., and Wetzstein, G. Confocal non-line-of-sight imaging based on the light-cone transform. *Nature 555*, 7696 (2018).

[27] Peabody, J. J. E., Charvat, G. L., Goodwin, J., and Tobias, M. Through-wall imaging radar. Tech. rep., MIT-Lincoln Laboratory, 2012.

[28] Qian, K., He, Z., and Zhang, X. 3d point cloud generation with millimeter-wave radar. *Proceedings of the ACM on Interactive, Mobile, Wearable and Ubiquitous Technologies* (2020).

[29] Qian, K., Yao, L., Zhang, X., and Ng, T. MilliMirror: 3D Printed Reflecting Surface for Millimeter-Wave Coverage Expansion. In *Proceedings of the Annual International Conference on Mobile Computing and Networking (MobiCom)* (2022).

[30] Qian, K., Yao, L., Zheng, K., Zhang, X., and Ng, T. N. UniScatter: a Metamaterial Backscatter Tag for Wideband Joint Communication and Radar Sensing. In *Proceedings of the ACM Annual International Conference on Mobile Computing and Networking* (2023).

[31] Qian, K., Zhu, S., Zhang, X., and Li, L. E. Robust multimodal vehicle detection in foggy weather using complementary lidar and radar signals. In *Proceedings of the IEEE/CVF Conference on Computer Vision and Pattern Recognition* (2021).

[32] Scheiner, N., Kraus, F., Wei, F., Phan, B., Mannan, F., Appenrodt, N., Ritter, W., Dickmann, J., Dietmayer, K., Sick, B., et al. Seeing around street corners: Non-line-of-sight detection and tracking in-the-wild using doppler radar. In *The IEEE Conference on Computer Vision and Pattern Recognition (CVPR)* (2020).

[33] Schubert, E., Kunert, M., Menzel, W., Fortuny-Guasch, J., and Chareau, J.-M. Human rcs measurements and dummy requirements for the assessment of radar based active pedestrian safety systems. In *International Radar Symposium (IRS)* (2013), vol. 2.

[34] Seidel, S., Rueda-Chacon, H., Cusini, I., Villa, F., Zappa, F., Yu, C., and Goyal, V. K. Non-line-of-sight tracking and mapping with an active corner camera, 2022.

[35] Selvan, K. T., and Janaswamy, R. Fraunhofer and fresnel distances : Unified derivation for aperture antennas. *IEEE antennas and propagation magazine 59*, 4 (2017).

[36] Setlur, P., Amin, M., and Ahmad, F. Multipath model and exploitation in through-the-wall and urban radar sensing. *IEEE Transactions on Geoscience and Remote Sensing 49*, 10 (2011).

[37] Shi, S., Cui, J., Jiang, Z., Yan, Z., Xing, G., Niu, J., and Ouyang, Z. Vips: real-time perception fusion for infrastructure-assisted autonomous driving. In *Proceedings of the 28th Annual International Conference on Mobile Computing And Networking* (2022), pp. 133–146.

[38] Sleasman, T., Boyarsky, M., Pulido-Mancera, L., Fromenteze, T., Imani, M. F., Reynolds, M. S., and Smith, D. R. Experimental synthetic aperture radar with dynamic metasurfaces. *IEEE Transactions on Antennas and Propagation 65*, 12 (2017).

[39] Solomitckii, D., Barneto, C. B., Turunen, M., Allén, M., Koucheryavy, Y., and Valkama, M. Millimeter-wave automotive radar scheme with passive reflector for blind corner conditions. In *European Conference on Antennas and Propagation (EuCAP)* (2020), IEEE.

[40] Solomitckii, D., Barneto, C. B., Turunen, M., Allén, M., Koucheryavy, Y., and Valkama, M. Millimeter-wave automotive radar scheme with passive reflector for blind corner conditions. In *European Conference on Antennas and Propagation (EuCAP)* (2020).

[41] Solomitckii, D., Barneto, C. B., Turunen, M., Allén, M., Zhabko, G. P., Zavjalov, S. V., Volvenko, S. V., and Valkama, M. Millimeter-wave radar scheme with passive reflector for uncontrolled blind urban intersection. *IEEE Transactions on Vehicular Technology 70*, 8 (2021).

[42] Solomitckii, D., Heino, M., Buddappagari, S., Hein, M. A., and Valkama, M. Radar scheme with raised reflector for nlos vehicle detection. *IEEE Transactions on Intelligent Transportation Systems* (2021).

[43] Soltanaghaei, E., Prabhakara, A., Balanuta, A., Anderson, M., Rabaey, J. M., Kumar, S., and Rowe, A. Millimetro: Mmwave retro-reflective tags for accurate, long range localization. In *Proceedings of the ACM Annual International Conference on Mobile Computing and Networking (MobiCom)* (2021).

[44] Sume, A., Gustafsson, M., Jänis, A., Nilsson, S., Rahm, J., and Örbom, A. Radar detection of moving objects around corners. In *Radar Sensor Technology XIII* (2009), International Society for Optics and Photonics.

[45] Sur, S., Pefkianakis, I., Zhang, X., and Kim, K.-H. Towards scalable and ubiquitous millimeter-wave wireless networks. In *Proceedings of the 24th Annual International Conference on Mobile Computing and Networking (MobiCom)* (2018).

[46] Sur, S., Zhang, X., Ramanathan, P., and Chandra, R. {BeamSpy}: Enabling robust 60 {GHz} links under blockage. In *13th USENIX symposium on*

networked systems design and implementation (NSDI) (2016).

[47] SWANSON, E. Geometric dilution of precision. *NAVIGATION, Journal of the Institute of Navigation 25*, 4 (1978).

[48] THAI, K.-P.-H., RABASTE, O., BOSSE, J., POULLIN, D., SÁENZ, I. D. H., LETERTRE, T., AND CHONAVEL, T. Detection–localization algorithms in the around-the-corner radar problem. *IEEE Transactions on Aerospace and Electronic Systems 55*, 6 (2019).

[49] ULUISIK, C., CAKIR, G., CAKIR, M., AND SEVGI, L. Radar cross section (rcs) modeling and simulation. *IEEE Antennas and Propagation Magazine* (2008).

[50] USFHWA. Maintaining traffic sign retroreflectivity: Impacts on state and local agencies. *Turner-Fairbank Highway Research Center* (2007).

[51] VELTEN, A., WILLWACHER, T., GUPTA, O., VEERARAGHAVAN, A., BAWENDI, M. G., AND RASKAR, R. Recovering three-dimensional shape around a corner using ultrafast time-of-flight imaging. *Nature communications 3*, 1 (2012).

[52] WAIT, J. R. Transmission and reflection of electromagnetic waves in the presence of stratified media. *J. Res. NBS 61*, 3 (1958), 205.

[53] WEI, T., WANG, S., ZHOU, A., AND ZHANG, X. Acoustic eavesdropping through wireless vibrometry. In *Proceedings of the ACM Annual International Conference on Mobile Computing and Networking (MobiCom)* (2015).

[54] WEI, T., ZHOU, A., AND ZHANG, X. Facilitating robust 60 ghz network deployment by sensing ambient reflectors. In *Proceedings of the USENIX Conference on Networked Systems Design and Implementation (NSDI)* (2017).

[55] WILLIAMS, A. The greedy gray code algorithm. In *Algorithms and Data Structures: 13th International Symposium, WADS 2013, London, ON, Canada, August 12-14, 2013. Proceedings 13* (2013), Springer, pp. 525–536.

[56] WOODFORD, T., ZHANG, X., CHAI, E., AND SUNDARESAN, K. Mosaic: Leveraging diverse reflector geometries for omnidirectional around-corner automotive radar. In *Proceedings of ACM Annual International Conference on Mobile Systems, Applications and Services (MobiSys)* (2022).

[57] WOODFORD, T., ZHANG, X., CHAI, E., SUNDARESAN, K., AND KHOJASTEPOUR, A. Spacebeam: Lidar-driven one-shot mmwave beam management. In *Proceedings of the Annual International Conference on Mobile Systems, Applications, and Services (MobiCom)* (2021), Association for Computing Machinery.

[58] WU, C., LIU, J., HUANG, X., LI, Z.-P., YU, C., YE, J.-T., ZHANG, J., ZHANG, Q., DOU, X., GOYAL, V. K., XU, F., AND PAN, J.-W. Non-line-of-sight imaging over 1.43 km. *Proceedings of the National Academy of Sciences (PNAS) 118*, 10 (2021).

[59] XIE, D., WANG, X., AND TANG, A. Metasight: localizing blocked rfid objects by modulating nlos signals via metasurfaces. In *Proceedings of the Annual International Conference on Mobile Systems, Applications and Services (MobiSys)* (2022).

[60] YI, H., QU, S.-W., NG, K.-B., CHAN, C. H., AND BAI, X. 3-d printed millimeter-wave and terahertz lenses with fixed and frequency scanned beam. *IEEE Transactions on Antennas and Propagation 64*, 2 (2015).

[61] YUE, S., HE, H., CAO, P., ZHA, K., KOIZUMI, M., AND KATABI, D. CornerRadar: RF-Based Indoor Localization Around Corners. *Proc. ACM Interact. Mob. Wearable Ubiquitous Technol. 6*, 1 (2022).

[62] ZHOU, A., XU, S., WANG, S., HUANG, J., YANG, S., WEI, T., ZHANG, X., AND MA, H. Robotic millimeter-wave wireless networks. *IEEE/ACM Transactions on Networking 28*, 4 (2020).